Research Article

Influence of Wave-Absorbing Chamber Width on the Wave Attenuation Performance of Perforated Caisson Sitting on Rubble-Mound Foundation

Peihong Zhao [ID]**, Dapeng Sun** [ID]**, and Hao Wu**

State Key Laboratory of Coastal and Offshore Engineering, Dalian 116024, Liaoning, China

Correspondence should be addressed to Peihong Zhao; 571509076@qq.com and Dapeng Sun; dpsun@dlut.edu.cn

A Jarlan-type perforated caisson consisted of a perforated front wall, a solid rear wall, and a wave-absorbing chamber between them. The wave-absorbing chamber was the main feature of the perforated caisson, and its width had a great effect on wave attenuation performance. In this study, a larger range of the wave-absorbing chamber width was observed in model experiments to investigate the effect on wave attenuation performance including the reflection coefficients and the horizontal wave forces of a perforated caisson sitting on a rubble-mound foundation. A resistance-type porosity numerical model based on the volume-averaged Reynolds-averaged Navier–Stokes (VARANS) equations was validated by comparing the present results with those of previously reported and present experiments. The validated numerical model was then used for extended research. It was found that the reflection coefficients, the total horizontal wave force, and its components all tended to oscillate in a decrease ⟶ increase ⟶ decrease manner with increasing the wave-absorbing chamber width. The reflection coefficients and wave forces acting on both sides of the perforated front wall were found to be synchronized regardless of perforation ratio or the rubble-mound foundation height.

1. Introduction

Perforated caissons were first proposed by Jarlan [1] in the 1960s. Since then, many researchers studied this coastal structure in analytical, physical, and numerical ways [2–8]. Some other new types of caisson were also proposed and studied in recent years [9, 10]. A Jarlan-type perforated caisson consisted of a perforated front wall, a solid rear wall, and a wave-absorbing chamber between them. When the incident wave overlapped with the reflected waves from the perforated front wall and the solid rear wall, the wave energy can be greatly reduced. Compared with the traditional caisson, a perforated caisson reduced reflection coefficients and the wave forces. In addition, a perforated caisson had the advantages of easy construction and a wide range of applications, making it a key structure in coastal and port engineering.

Chen et al. [11], Ma et al. [12], and Jiang et al. [13, 14] carried out physical model experiments to study the irregular wave interaction with a perforated caisson breakwater on an impermeable and a permeable seabed. In those experiments, the relative wave-absorbing chamber width was between 0.064 and 0.208. It was pointed out that both the reflection coefficients and the horizontal wave forces acting on a perforated caisson were both correlated quadratically with the wave-absorbing chamber width, but this conclusion had not been confirmed for a perforated caisson sitting on a rubble-mound foundation. Xing [15] studied the irregular wave interaction with a perforated caisson breakwater on a rubble-mound foundation of three different heights, with the wave-absorbing chamber width between 0.064 and 0.208. Within this range, both the reflection coefficients and the horizontal wave forces acting on a perforated caisson were also correlated quadratically with the wave-absorbing chamber width.

So far, it is generally believed that the wave-absorbing chamber width is one of the key factors affecting the wave attenuation performance of a perforated caisson sitting on

on a rubble-mound foundation. However, when the wave-absorbing chamber width expanded to a larger range, can the changes in reflection coefficients and horizontal wave forces still be described by a quadratic function? Most experimental studies on perforated caissons limit the wave-absorbing width to a small range, so this problem was not solved. Liu et al. [16] attempted to analytically calculate the reflection coefficients of a perforated caisson based on potential flow theory. In their research, the perforated caisson was bedded on an impermeable step, which differs from a rubble-mound foundation used in engineering practice; therefore, the applicability of their analytical solution had great limitations.

Accordingly, in this study, by giving a larger range of the wave-absorbing chamber width, model experiments were carried out to study the effect of the wave-absorbing chamber width on the attenuation performance of a perforated caisson sitting on a rubble-mound foundation. Meanwhile, a resistance-type porosity numerical model based on the volume-averaged Reynolds-averaged Navier–Stokes (VARANS) equations was validated by comparing the present results with those of previously reported and present experiment. The validated numerical model was then used for extended research.

2. Numerical Model

In the present research, the resistance-type porosity model proposed by Zhao [17] was adopted. This numerical model used the VARANS equations to uniformly describe the flow inside and outside the porous structure, as well as a volume-averaged $k - \varepsilon$ model to simulate the turbulence effect. In addition, the three-step finite element method (FEM) was applied to solve the VARANS equations numerically, and the computational Lagrangian–Eulerian advection remap-volume of fluid (CLEAR-VOF) method was applied to capture the free water surface. In the following sections, the governing equations, calibration of the resistance coefficients, and validation process were explained.

2.1. VARANS Equations. Figure 1 shows the definition of a porous medium. The surface S for generating the averaging volume V included a solid phase and a fluid phase. S was defined by a circle with the radius r_0. The actual volume of the fluid phase V_f varied with the porous medium based on the position of the averaging volume, while the total volume V was constant. The macroscopic length scale L and the pore length scale l were also shown in this figure.
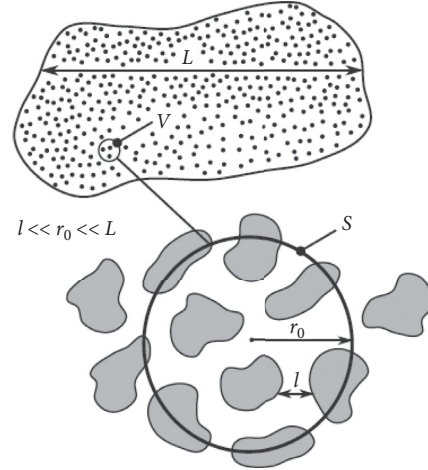

Figure 1: Definition of volume average areas and length scales.

A volume averaging procedure was applied to convert Reynolds-averaged Navier–Stokes (RANS) equations to VARANS equations, and the length scale constraint was given as $l << r_0 << L$. The superficial volume average denoted by $\langle \ \rangle$ was defined as the average over the entire volume. The intrinsic average denoted by $\langle \ \rangle^f$ was defined as the average over the fluid volume. The superficial and intrinsic volume averages of a scalar, vector, or tensor denoted by B were defined as follows:

$$\langle B \rangle = \frac{1}{V} \int_{V_f} B \mathrm{d}V,$$
$$\langle B \rangle^f = \frac{1}{V_f} \int_{V_f} B \mathrm{d}V. \tag{1}$$

The relation between these two averages was as follows:

$$\langle B \rangle = n \langle B \rangle^f, \tag{2}$$

where n was the porosity given by

$$n = \frac{V_f}{V}. \tag{3}$$

In order to obtain VARANS equations, Navier–Stokes equations were ensemble averaged by applying a time-average operator to obtain the Reynolds-averaged Navier–Stokes (RANS) equations. Then, a volume-average operator was applied to the RANS equations to obtain volume-averaged Reynolds-averaged Navier–Stokes (VARANS) equations:

$$\frac{\partial \langle \overline{u}_i \rangle}{\partial x_i} = 0, \tag{4}$$

$$\frac{\partial \langle \overline{u}_i \rangle}{\partial t} + \frac{\langle \overline{u}_j \rangle}{1 + c_m} \frac{\partial}{\partial x_j} \frac{\langle \overline{u}_i \rangle}{n} = -\frac{n}{1 + c_m} \frac{\partial}{\partial x_i} \frac{\langle \overline{p} \rangle^f}{\rho} + \frac{n}{1 + c_m} \frac{\partial}{\partial x_j} \left(\nu + \langle \nu_t \rangle \right) \left(\frac{\partial}{\partial x_j} \frac{\langle \overline{u}_i \rangle}{n} + \frac{\partial}{\partial x_i} \frac{\langle \overline{u}_j \rangle}{n} \right) + \frac{n g_i}{1 + c_m} - \frac{f_i}{1 + c_m}, \tag{5}$$

where f_i along with the inertia term was the extended Darcy–Forchheimer resistance term F_i defined as follows:

$$nF_i = f_i + c_m \frac{\partial}{\partial t} \langle \overline{u}_i \rangle = a\langle \overline{u}_i \rangle + b|\langle \overline{\mathbf{u}} \rangle| u_i + c_m \frac{\partial}{\partial t} \langle \overline{u}_i \rangle. \quad (6)$$

The first term on the right-hand side of equation (6) was the linear resistance term, and the second term was the quadratic resistance term. a and b were experimental coefficients that need to be determined in advance. The last

term was the inertia term. $c_m = 0.34(1\text{-}n)/n$ was the added mass coefficient representing the transient interaction between grain and water. It was obvious that $n = 1$ and $c_m = 0$ outside the porous media, and then VARANS equations automatically changed back to RANS equations.

In equation (5), $\langle v_t \rangle = C_\mu \langle k \rangle^2 / \langle \varepsilon \rangle$ was the volume-averaged eddy viscosity, and the balance equations of $\langle k \rangle$ and $\langle \varepsilon \rangle$ were obtained by taking the volume averaging over the standard k and ε equations which turn to the following:

$$\frac{\partial}{\partial t} \langle k \rangle + \langle \overline{u}_j \rangle \frac{\partial}{\partial x_j} \frac{\langle k \rangle}{n} = 2v_t n \langle S_{ij} \rangle^f \langle S_{ij} \rangle^f - \langle \varepsilon \rangle + n \frac{\partial}{\partial x_j} \left[\left(v + \frac{v_t}{n\sigma_k} \right) \frac{\partial}{\partial x_j} \frac{\langle k \rangle}{n} \right] + n\varepsilon_\infty, \quad (7)$$

$$\frac{\partial}{\partial t} \langle \varepsilon \rangle + \langle \overline{u}_j \rangle \frac{\partial}{\partial x_j} \frac{\langle \varepsilon \rangle}{n} = 2v_t n C_{\varepsilon1} \frac{\langle \varepsilon \rangle}{\langle k \rangle} \langle S_{ij} \rangle^f \langle S_{ij} \rangle^f + C_{\varepsilon2} \frac{\langle \varepsilon \rangle^2}{\langle k \rangle} + n \frac{\partial}{\partial x_j} \left[\left(v + \frac{v_t}{n\sigma_k} \right) \frac{\partial}{\partial x_j} \frac{\langle \varepsilon \rangle}{n} \right] + n C_{\varepsilon2} \frac{\varepsilon_\infty^2}{k_\infty}, \quad (8)$$

where

$$\langle S_{ij} \rangle^f = \frac{1}{2} \left(\frac{\partial}{\partial x_j} \frac{\langle \overline{u}_i \rangle}{n} + \frac{\partial}{\partial x_i} \frac{\langle \overline{u}_j \rangle}{n} \right). \quad (9)$$

In equations (7) and (8), $\sigma_k = 1.00$, $\sigma_\varepsilon = 1.30$, $C_{\varepsilon1} = 1.44$, and $C_{\varepsilon2} = 1.92$ as Nakayama and Kuwahara [18] (1999) suggested. k_∞ and ε_∞ were additional sources of turbulence due to the presence of porous materials. They represented small-scale turbulence that was smaller than the averaging volume. Nakayama and Kuwahara [18] also proposed closure schemes for small-scale turbulence based on the numerical simulation of a fluid flowing through a series of square rods:

$$\varepsilon_\infty = 39.0 \frac{(1-n)^{(5/2)}}{n} \frac{|\langle \overline{\mathbf{u}} \rangle|^3}{d_{50}},$$

$$k_\infty = 3.7 \frac{1-n}{\sqrt{n}} |\langle \overline{\mathbf{u}} \rangle|^2. \quad (10)$$

2.2. Calibration Methods for Experimental Coefficients in VARANS Equations.
According to Forchheimer's research, the Darcy–Forchheimer resistance coefficients a and b occurred in equation (6) were related to the permeability of the porous medium. They were expressed as $a = \mu/\rho K$ and $b = C_F/\sqrt{K}$, respectively, where μ was the coefficient of kinematic viscosity of the fluid, K was the permeability of the porous medium, which could be written as $K = n^3 d_{50}^2 / \alpha(1 - n)^2$, and C_F was an unknown coefficient, which could be written as $C_F = \beta/\sqrt{\alpha n^3}$. Thus, a and b could be expressed as $a = \alpha\mu(1 - n)^2/\rho n^3 d_{50}^2$ and $b = \beta(1 - n)/n^3 d_{50}$ equivalently, where d_{50} was the mean diameter (or grain diameter if the porous medium was homogeneous) of the porous medium and both α and β were coefficients related to the microscopic geometry of the porous medium. When numerically simulating a specific experimental model, the mean diameter d_{50} and porosity n could usually be measured. However, α and β were

unknown, and they had to be determined through certain calibration procedures.

It should be noted that research studies gave different values depending on how the coefficients were determined or calibrated, how the resistance coefficients a and b were formulated, and even how the numerical model handled turbulence effects. Zhao [17] proposed a calibration method, that was, when using different values of α and β, the wave damping rate of wave motion over porous seabed could be regarded as an index to evaluate the accuracy of numerical simulation. Although the wave motion over the porous seabed was a dynamic process, after a period of time, the entire damping system became stable, and wave heights along the distance remained unchanged. The total error could be expressed as follows:

$$\varepsilon = \frac{|k_i^{\text{exp}} - k_i^{\text{num}}|}{k_i^{\text{exp}}}, \quad (11)$$

where k_i^{exp} was the wave damping rate measured in experiments; k_i^{num} was the wave damping rate calculated by numerical modeling; and ε was the relative error. It was seen that the wave damping rate was the only parameter required in the error estimation procedure, which made this calibration method proposed by Zhao [17] easier to implement. In this paper, the same calibration method was adopted and the coefficients α and β were determined to be 100 and 2.0, respectively.

2.3. Validation Using the Existed Model Experiments.
The numerical model proposed by Zhao [17] could be successfully used to simulate the porous media-fluid coupled flow. By comparing the simulation results with the existing model experimental results, the applicability and accuracy of the simulation of the irregular wave interaction with a perforated caisson sitting on a rubble-mound foundation were validated.

Xing et al. [15] studied the irregular wave interaction with a perforated caisson breakwater on a rubble-mound

foundation. In their model experiments, the widths of the wave chamber b_c were set to 0.15, 0.20, and 0.30 m. The front wall of the caisson was partially perforated from 0.2 m below the water surface to the top of the caisson. The porosity μ of the perforated front wall was set to 20% and 40%. The water depth d during the test was maintained at 0.4 m. The heights of the rubble-mound foundation h_m were set to 0.10 m, 0.15 m, and 0.20 m. The berm width of the foundation W was 0.25 m. The core of the rubble-mound foundation was the same as the rock-fill core in the wave-absorbing chamber. The grain diameter d_{50} was about 1.1 cm, and the porosity of the core n was about 0.4. The significant wave height H_s was 0.053 m. Because the water depth d during the test was maintained at 0.4 m, the significant wave lengths L_s were only related to the wave periods. They were 2.35 m, 1.82 m, and 1.44 m, respectively, when the significant wave periods T_s were 1.38 s, 1.15 s, and 0.99 s. After combining all these varied factors, a total of 54 cases were carried out in their work.

As shown in Figure 2, a 2-D numerical wave flume was developed in this study. The length of the flume is 15 m. The left boundary represents the wave-maker, and the boundary condition is the velocity inlet. The rubble-mound foundation and the perforated caisson sitting on it were located in the middle section of the wave flume. The perforated front wall was 7.7 m away from the left boundary, which made the left side of the perforated wall the seaward side and the right side the leeward side.

In order to eliminate the effect of re-reflect waves between the structure and the wave generator, a time-domain method for separating the incident waves and the reflected waves (SIRW method) by Frigaard and Christensen [19, 20] was adopted in the present research. It was proved that this method could be used in investigating the irregular wave interaction with a perforated caisson by Tang [21]. In addition, a sponge layer was located on the right side of the wave flume, and the flow velocity in it decayed exponentially.

An irregular wave train could be treated as a stationary stochastic process. It was assumed to be a linear superposition of large numbers of monochromatic wave components with different wave heights, wave angular frequencies, and random initial phases. The incident wave spectrums of experiments and numerical modeling were both the modified JONSWAP spectrum (Goda, 1999 [22]). So, by neglecting the interaction of different component of waves, the reflection coefficient of each component could be calculated by estimation of incident and reflected waves [23]. Once the reflection coefficient of each component was determined, the reflected spectral density was obtained by

$$S_r\left(\omega_j\right) = K_{rj} S_i\left(\omega_j\right), \tag{12}$$

where K_{rj} was the reflection coefficient of the jth component and $S_r(\omega_r)$ and $S_r(\omega_j)$ were the spectral densities of the reflected and incident waves, respectively. For irregular waves, the average reflection coefficient Kr can be calculated by

$$\overline{K}_r = \sqrt{\frac{m_{0,r}}{m_{0,i}}}, \tag{13}$$

where $m_{0,r}$ and $m_{0,I}$ are the zero-order moments of the reflected and incident wave spectra, respectively, and can be calculated by

$$\begin{aligned} m_{0,r} &= \int_0^\infty S_r\left(\omega\right)\mathrm{d}\omega, \\ m_{0,i} &= \int_0^\infty S_i\left(\omega\right)\mathrm{d}\omega. \end{aligned} \tag{14}$$

For consistency, the average reflection coefficient Kr was considered as the reflection coefficient of irregular waves and just be written as Kr in the following sections.

In order to accurately calculate the reflection coefficient of each component of waves, five wave height gauges (numbered $1^\#$ to $5^\#$) were arranged 2.8 m, 3.1 m, 3.6 m, 3.91 m, and 4.17 m from the seaward face of the caisson, respectively. Appropriate combination of wave gauges was to be selected according to different wave length of each component of waves.

The accuracy of the numerical model could be illustrated by comparing the time series data of wave elevation or the frequency spectrum based on numerical modeling and experimental results. For instance, Figure 3 shows a target spectrum of the irregular wave in experiments and numerical modeling for $L_s = 1.82$ m; Figure 4 shows both the numerical and experimental time series data of wave elevation and the corresponding frequency spectrum measured by the $1^\#$ wave height gauge for $h_m = 0.15$ m; $b_c = 0.2$ m; $\mu = 0.4$; and $L_s = 1.82$ m. It was seen that the numerical results were in good agreement with the experimental results. Only in the high frequency region, some deviation occurred.

In Figure 5, the reflection coefficients Kr calculated based on the numerical and experimental results were compared, where the horizontal axis represented the relative wave-absorbing chamber width b_c/L_s. It was seen that in Xing's model experiments, the relative wave-absorbing chamber width was about 0.064–0.208, and within this range, K_r varied nonlinearly. In some cases, as shown in Figure 5(f), the minimum of K_r was found. Therefore, a quadratic function was used to describe the correlation between K_r and the relative wave-absorbing chamber width. The curves for the three h_m values were calculated from the formula proposed by Xing et al. [15].

In general, Figure 5 indicated a reasonable agreement between the numerical and experimental values of K_r in all 54 cases. The numerical model used in the present research was applicable and sufficiently accurate to simulate the wave interaction with a perforated caisson sitting on a rubble-mound foundation.

3. Effect of the Wave-Absorbing Chamber Width on the Wave Attenuation Performance

As mentioned in the previous section, since the range of the wave-absorbing chamber width was very small, within this range, it was reasonable to use a quadratic function to describe the variation of reflection coefficients. However, when the wave-absorbing chamber width continued to increase, what would be the behavior of the reflection
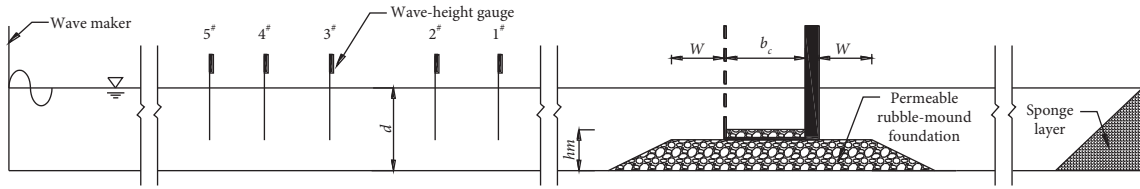
Figure 2: 2-D numerical wave flume and the perforated caisson sitting on the rubble-mound foundation.
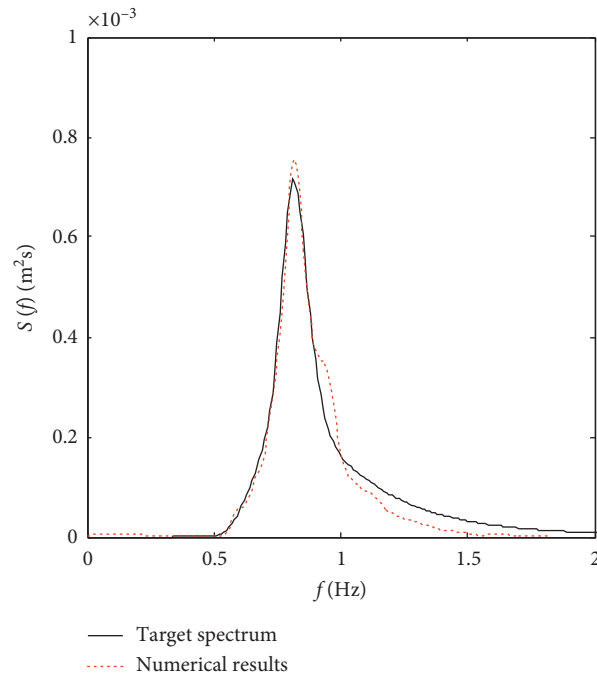

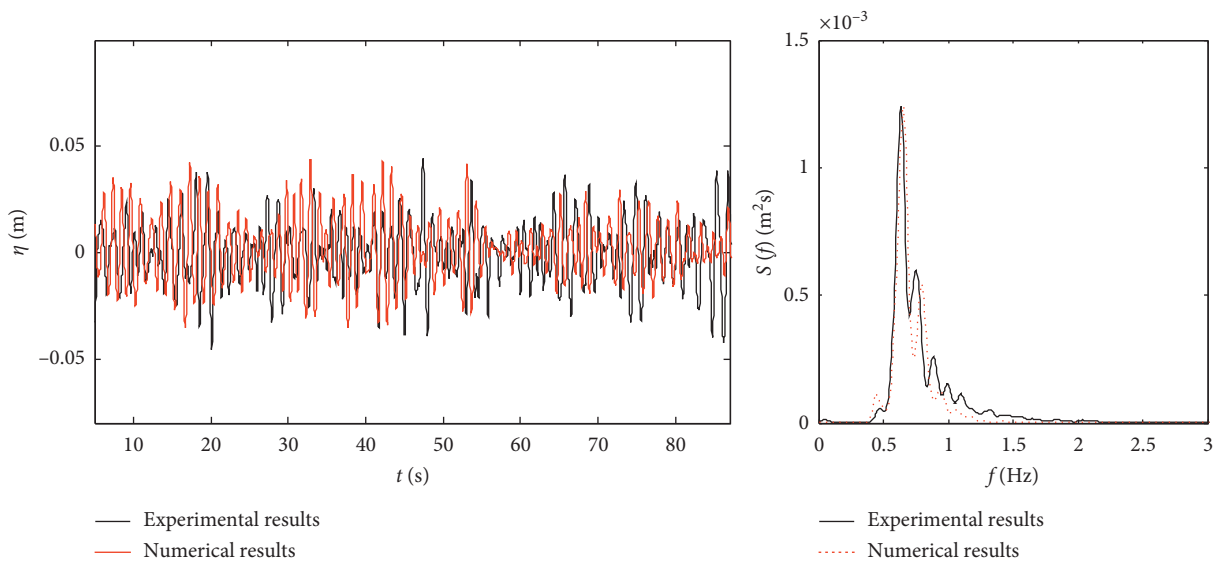Figure 3: 1# target spectrum of irregular wave and the numerical results.

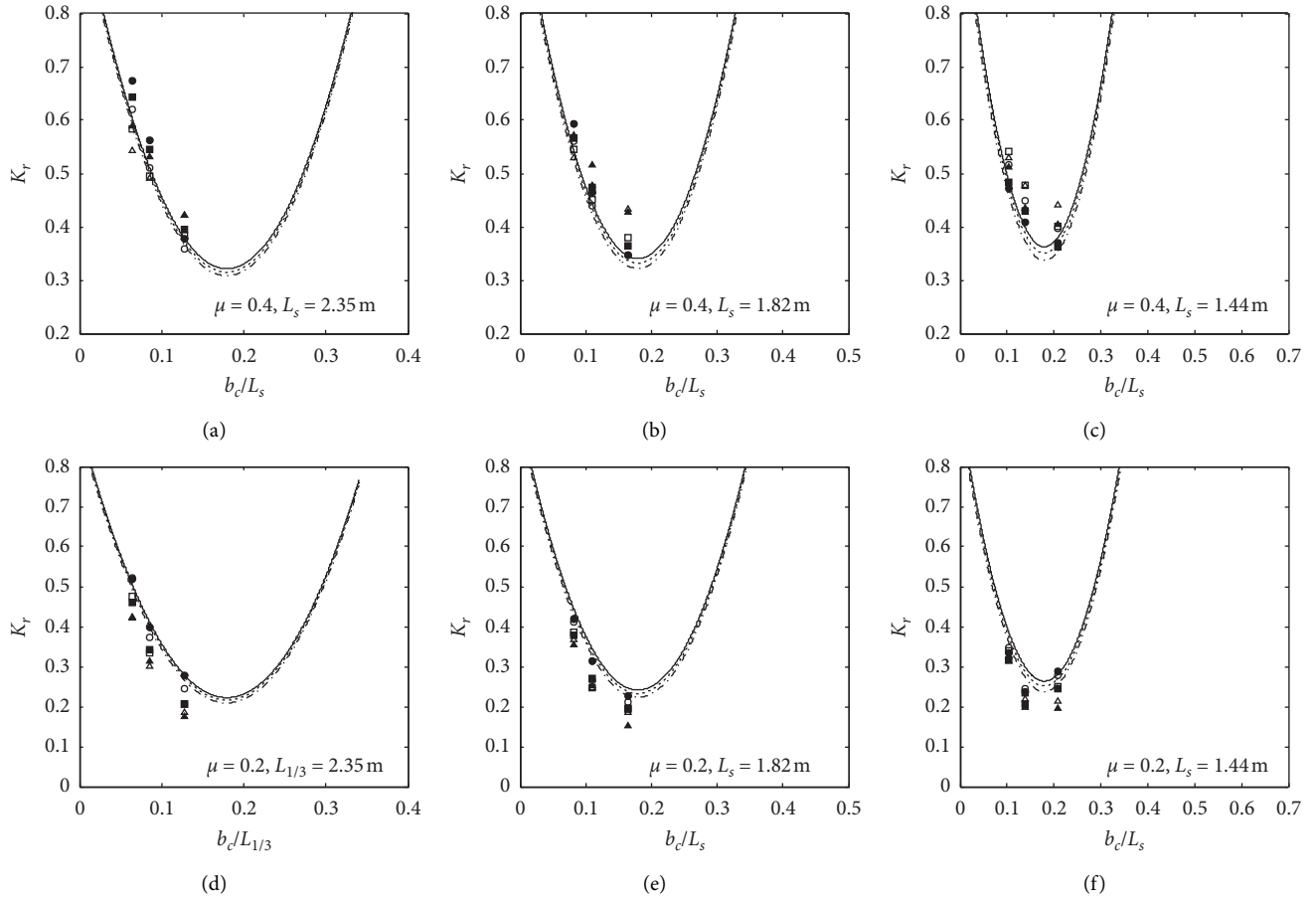Figure 4: 1# time series data of wave elevation and frequency spectrum.

FIGURE 5: Comparison of the reflection coefficient K_r: ●, experimental results as $h_m = 0.10$ m; ○, numerical results as $h_m = 0.10$ m; (—), calculation results by Xing as $h_m = 0.10$ m; ■, experimental results as $h_m = 0.15$ m; □, numerical results as $h_m = 0.15$ m; (--), calculation results by Xing as $h_m = 0.15$ m; ▲, experimental results as h $h_m = 0.20$ m; △, numerical results as $h_m = 0.20$ (m) (-.), calculation results by Xing as $h_m = 0.20$ m.

coefficient and even the horizontal wave force acting on the perforated caisson sitting on the rubble-mound foundation? In this paper, model experiments and numerical simulations were used to answer this question.

3.1. Model Experiments and Numerical Simulations.
The model experiments were carried out at the State Key Laboratory of Coastal and Offshore Engineering, Dalian University of Technology. The wave flume was 56 m in length and 0.7 m in width. A hydraulic servo push-plate type wave generator was installed on one side of the flume. An anti-slope device was installed on the other side to dissipate wave energy. The setup of the wave height gauges was the same as in Xing et al. [15].

The roofless caisson was made of PMMA with a thickness of 1 cm. Four rows of uniformly distributed rectangular holes were cut out from 0.2 m below the water surface to the top of the caisson, which led to a perforation ratio μ of 40%. The height of the rubble-mound foundation h_m was set to 0.20 m. In these experiments, the range of wave-absorbing chamber width b_c was very large, measuring 0.15, 0.20, 0.30, 0.40, 0.50, 0.60, 0.70, and 0.80 m. The perforated caisson model is shown in Figure 6.

In order to calculate the wave forces on the caisson, pressure gauges were installed on both sides of the perforated front wall and the solid rear wall, as shown in Figure 7. Once the time series data of pressure were collected, the horizontal wave forces acting on each wall and the total horizontal wave forces acting on the entire structure could be calculated by a simple integration algorithm.

In the whole experiment, the significant wave height H_s was 0.053 m, and other geometric parameters and wave experimental conditions are shown in Table 1. The numerical model validated in the previous section was adopted here to simulate the model experiment cases.

3.1.1. Reflection Coefficients.
Figure 8 shows the obtained numerical and experimental reflection coefficients as the wave-absorbing chamber width varied from 0.15 m to 0.80 m. In Figures 8(a)–8(c), three different groups of cases with the significant wave lengths $L_s = 2.35$ m, 1.82 m, and 1.44 m were shown, respectively. It was seen that the numerical results were in good agreement with the experimental results. Results showed that resonant conditions occurred for various b_c/L_s values introducing an oscillation
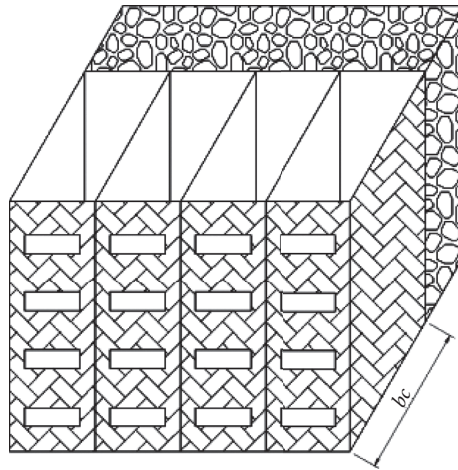
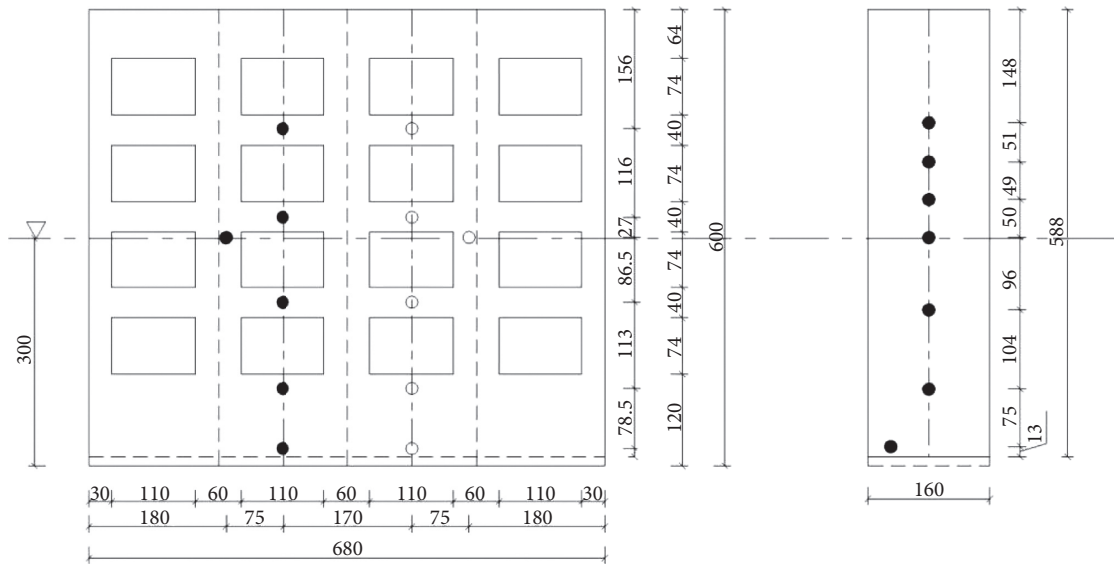FIGURE 6: The perforated caisson used in the experiments.

FIGURE 7: Perforated front wall and solid rear wall of the caisson: ●, pressure gauges on the seaward side of the front perforated wall and the solid rear wall; ○, pressure gauges on the leeward side of the perforated front wall.

TABLE 1: Experimental conditions and geometric parameters.

Significant wave period T_s (s)	1.38, 1.15, 0.99
Chamber width b_c (m)bc	0.15, 0.20, 0.30, 0.40, 0.50, 0.60, 0.70, 0.80
Foundation height h_m (m)	0.20
Relative foundation height h_m/L_s hm/L1/3	0.043~0.139
Relative chamber width b_c/L_s bc/L1/3	0.064~0.590
Relative water depth d/L_s d/L1/3	0.17~0.278

in a decrease ⟶ increase ⟶ decrease manner of the reflection coefficients.

This indicated that for incident waves with the same periods, as the wave-absorbing chamber width increased, the phase differences between the incident wave, the wave reflected from the perforated front wall, and the solid rear wall oscillated. This oscillation behavior is most clearly seen in Figure 8(c) in which the significant wave length L_s was the shortest, and the range of the relative wave-absorbing chamber width b_c/L_s was therefore largest. According to
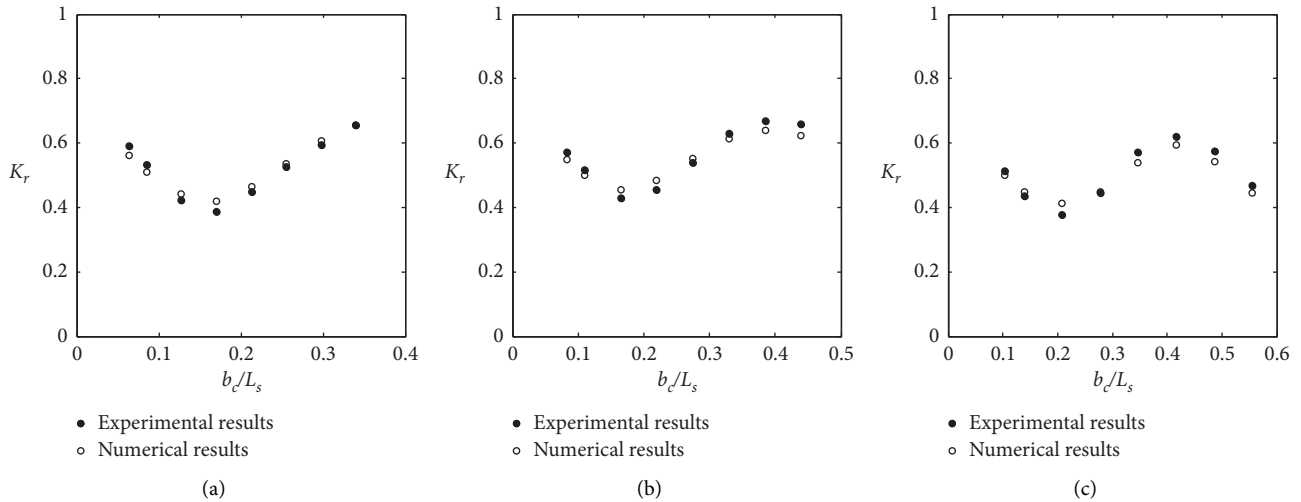
FIGURE 8: Experimental and numerical reflection coefficients.

Figure 8, for a greater range of the wave-absorbing chamber width changed, a quadratic function could no longer describe the correlation between the relative wave-absorbing chamber width and reflection coefficients; therefore, the formula of Xing [15] did not apply in such cases.

3.1.2. Horizontal Wave Forces.

Another important subject for studying the wave attenuation performance of a perforated caisson sitting on a rubble-mound foundation was the horizontal wave force. This subject included the horizontal wave forces acting on each wall of a perforated caisson and the total horizontal wave force acting on the entire structure. For a typical Jarlan-type perforated caisson, the total horizontal wave force F_h could be decomposed into three different components, as shown in Figure 9(a). The total horizontal wave force could be expressed as $F_h = F_{h1} - F_{h2} + F_{h3}$, where F_{h1} represented the wave force acting on the seaward side of the perforated front wall, F_{h2} was the force acting on the leeward side of the perforated front wall, and F_{h3} was the force acting on the solid rear wall.

Under the same conditions, F_{h0} was the horizontal wave force acting on a traditional caisson, as shown in Figure 9(b).

To study the horizontal wave forces acting on each part of the perforated caisson, dimensionless ratio parameters F_{h1}/F_{h0}, F_{h2}/F_{h0}, and F_{h3}/F_{h0} were introduced. The dimensionless total horizontal wave force could be expressed by F_h/F_{h0}. Since F_{h2} was opposite in direction to F_{h0}, F_{h2}/F_{h0} was always negative. Figure 10 shows the numerical and experimental horizontal wave forces as the wave-absorbing chamber width varied from 0.15 m to 0.80 m. In Figures 10(a)–10(c), three different groups of cases with the significant wave lengths $L_s = 2.35$ m, 1.82 m, and 1.44 m were shown, respectively. It could be seen that the numerical results were in good agreement with the experimental results. Based on the numerical results, spline curves are used to smooth the curves in Figure 10 and in other graphs in the following sections.

As the wave-absorbing chamber width increased over a large range, results showed that resonant conditions occurred for various b_c/L_s values introducing an oscillation in a decrease $\longrightarrow$ increase $\longrightarrow$ decrease manner of all F_{h1}/F_{h0}, F_{h2}/F_{h0}, and F_{h3}/F_{h0}. The oscillation of curves of F_{h1}/F_{h0} and F_{h2}/F_{h0} indicated that for incident waves with the same periods, as the wave-absorbing chamber width increased, the phase differences between the incident wave, the wave reflected from the perforated front wall, and the solid rear wall oscillated. The oscillation of F_{h3}/F_{h0} curve indicated that for incident waves with the same periods, as the wave-absorbing chamber width increased, the phase differences between the incident wave, the wave reflected from the solid rear wall, and the re-reflected wave from the leeward side of the perforated front wall oscillated. The curve of F_{h2}/F_{h0} showed the most obvious oscillation, and the oscillating amplitude of the F_{h1}/F_{h0} curve was smaller than that of F_{h2}/F_{h0}. This indicated that the wave forces acting on the seaward and the leeward side of the perforated front wall of the caisson varied asymmetrically with the increase in the wave-absorbing chamber width.

It must be noted that synchronization could be found when investigating the curves of F_{h1}/F_{h0}, F_{h2}/F_{h0}, and K_r. This meant that when K_r reached its maximum or minimum value, F_{h1}/F_{h0} and F_{h2}/F_{h0} also simultaneously reached their maximum or minimum values. On the other hand, the F_{h3}/F_{h0} curve showed some hysteresis.

Figure 11 shows the numerical and experimental values of the total horizontal wave force as the wave-absorbing chamber width varied from 0.15 m to 0.80 m. In Figures 11(a)–11(c), three different groups of cases with the significant wave lengths $L_s = 2.35$ m, 1.82 m, and 1.44 m were shown, respectively. Some differences can be seen but generally the numerical results were consistent with the experimental results.

Results showed that resonant conditions occurred for various b_c/L_s values introducing an oscillation in a decrease $\longrightarrow$ increase $\longrightarrow$ decrease manner of F_h/F_{h0}. Compared with the curves of F_{h1}/F_{h0} and F_{h2}/F_{h0}, the F_h/F_{h0} curve was more similar to the F_{h3}/F_{h0} curve. This was because, on the one hand, the horizontal wave force acting on
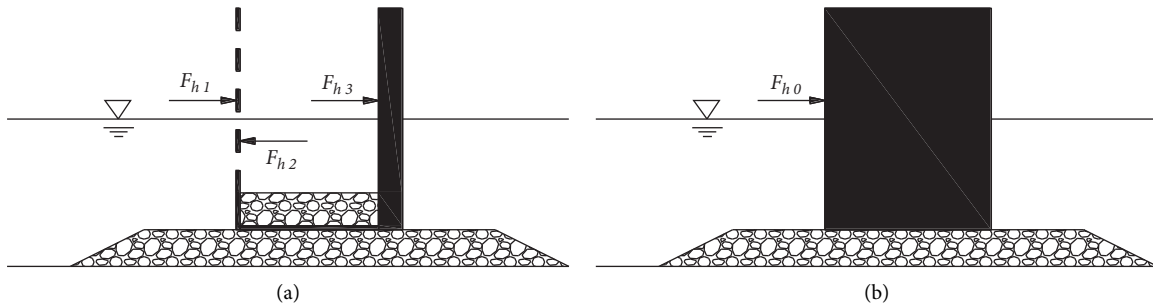
FIGURE 9: Wave forces acting on (a) perforated and (b) traditional caisson sitting on a rubble-mound foundation.
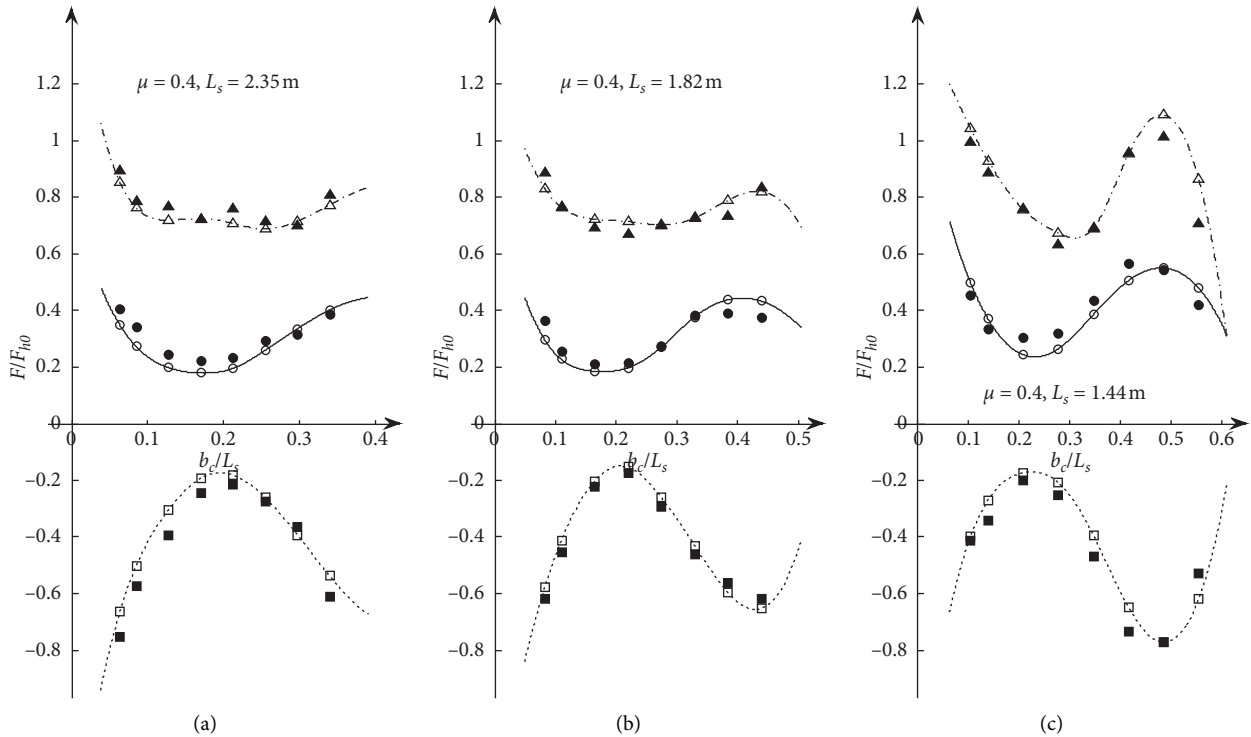

FIGURE 10: Horizontal wave forces acting on each part of the perforated caisson with irregular waves: black ○, numerical results of F_{h1}/F_{h0}; black ●, experimental results of F_{h1}/F_{h0}; black □, numerical results of F_{h2}/F_{h0}; black ■, experimental results of F_{h2}/F_{h0}; black △, numerical results of F_{h3}/F_{h0}; black ▲, experimental results of F_{h3}/F_{h0}.
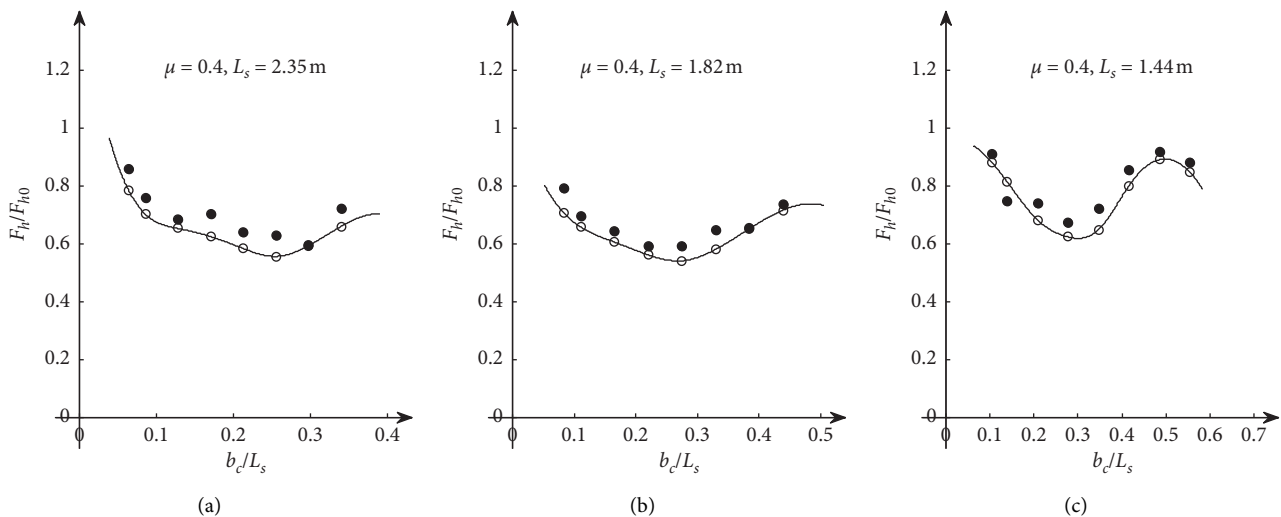

FIGURE 11: Total horizontal wave force acting on the perforated caisson with irregular waves: black ○, numerical results of F_h/F_{h0}.; black ●, experimental results of F_h/F_{h0}.

the solid rear wall was always larger than that acting on the perforated front wall under experimental conditions. On the other hand, the wave force acting on the seaward side of the perforated front wall was offset by that acting on the leeward side, so the contribution to the total horizontal force was rather small.

In general, for all values of reflection coefficient K_r, the total horizontal wave force or its components, results showed that resonant conditions occurred for various b_c/L_s values introducing an oscillation in a decrease $\longrightarrow$ increase $\longrightarrow$ decrease manner. It was clear that their relationships could not be described by a quadratic function.

3.2. Extended Research Using the Numerical Model.
The experimental cases mentioned in the previous section were limited. In fact, this experiment only included the cases of rubble-mound foundation height $h_m = 0.2$ m and the perforation ratio $\mu = 0.4$. In other cases, how would the reflection coefficient K_r, the total horizontal wave force, and its components vary as the wave-absorbing chamber width increased? Would there be any similarities or differences? To answering these questions, the numerical model was used for extended research to extrapolate the above results beyond the parameters of the model experiments.

Different cases with three rubble-mound foundation heights, two perforation ratios, eight wave-absorbing chamber widths, and three significant wave lengths were considered. It totally included 144 cases after combing all these factors. Table 2 showed all the modeling conditions and geometric parameters.

3.2.1. Effect of Wave-Absorbing Chamber Width on Reflection Coefficients.
Figure 12 shows the obtained numerical and experimental reflection coefficients as the wave-absorbing chamber width varied from 0.15 m to 0.80 m. Three different groups of cases with the significant wave lengths $L_s = 2.35$ m, 1.82 m, and 1.44 m were shown, respectively. In Figures 12(a)–12(c), the perforation ratio was 0.4. In Figures 12(d)–12(f), the perforated ratio was 0.2.

Generally, as the wave-absorbing chamber widened, the reflection coefficients tended to oscillate in a decrease $\longrightarrow$ increase $\longrightarrow$ decrease manner. This was a common feature regardless of the rubble-mound foundation height or the perforation ratio.

From Figures 12(a)–12(c), it was found that when the perforated ratio $\mu = 0.4$, the oscillating amplitude became smaller for higher foundations. However, in Figures 12(d)–12(f), this phenomenon was not evident.

Comparison between Figures 12(a), 12(b), and 12(c) with 12(d), 12(e), and 12(f) in that order showed that as the wave-absorbing chamber width increased, different perforation ratios also resulted in different amplitudes of the oscillating curves.

3.2.2. Effect of Wave-Absorbing Chamber Width on the Horizontal Wave Forces.
Figure 13 shows the numerical and experimental horizontal wave forces acting on each part of

Table 2: Numerical modeling conditions and geometric parameters.

Significant wave period T_s (s)	1.38, 1.15, 0.99
Significant wave length L_s (m)	2.35, 1.82, 1.44
Chamber width b_c (m)	0.15, 0.2, 0.3, 0.4, 0.5, 0.6, 0.7, 0.8
Foundation height h_m (m)	0.10, 0.15, 0.20
Perforation ratio μ	$0.2 \sim 0.4$
Relative foundation height $h_m/L_{1/3}$	$0.043 \sim 0.139$
Relative chamber width $b_c/L_{1/3}$	$0.064 \sim 0.556$
Relative water depth $d/L_{1/3}$	$0.17 \sim 0.278$

the perforated caisson as the wave-absorbing chamber width varied from 0.15 m to 0.80 m. Three different groups of cases with the significant wave lengths $L_s = 2.35$ m, 1.82 m, and 1.44 m were shown, respectively. In Figures 13(a)–13(c), the perforated ratio was 0.4, and in Figures 13(d)–13(f), the perforated ratio was 0.2.

Generally, as the wave-absorbing chamber width increased, F_{h1}/F_{h0}, F_{h2}/F_{h0}, and F_{h3}/F_{h0} tended to oscillate in a decrease $\longrightarrow$ increase $\longrightarrow$ decrease manner. The F_{h2}/F_{h0} curve oscillated most obviously, and the oscillating amplitude of F_{h1}/F_{h0} was smaller than that of F_{h2}/F_{h0}. Synchronization occurred between F_{h1}/F_{h0}, F_{h2}/F_{h0}, and K_r to some extent that they reached their maxima and minima simultaneously. However, F_{h3}/F_{h0} showed some hysteresis. These features were seen regardless of rubble-mound foundation height or the perforation ratio.

For different perforation ratios, it could be found that when $\mu = 0.4$, the horizontal wave force acting on the seaward side of the perforated front wall was smaller than that for $\mu = 0.2$. Conversely, the horizontal wave force acting on the solid rear wall was greater. This was mainly because the perforation ratio of the front wall determined how much incident wave energy passed into the wave-absorbing chamber and how much was reflected from the front wall. When the perforation ratio was small, less wave energy entered, which meant that the perforated front wall was subject to greater horizontal wave forces. In addition, compared with the case of $\mu = 0.4$, the curves of F_{h1}/F_{h0} and F_{h3}/F_{h0} were flatter near their minima and change more sharply when they began to climb or fall. When $\mu = 0.2$, the curves were less symmetrical than for $\mu = 0.4$.

By comparing figures with different rubble-mound foundation heights, it could be found that the rubble-mound foundation height had limited influence on the horizontal wave forces. When h_m became higher, F_{h1}/F_{h0} gets smaller only on the seaward side of the perforated front wall. This indicated that the horizontal wave forces acting on the area close to the bottom of the caisson were very small. In addition, some deviation was found in the F_{h2}/F_{h0}, curves when $h_m = 0.2$ m especially near their maxima.

Figure 14 shows the numerical and experimental total horizontal wave forces as the wave-absorbing chamber width varied from 0.15 m to 0.80 m. Three different groups of cases with the significant wave lengths $L_s = 2.35$ m, 1.82 m, and 1.44 m were shown, respectively. In Figures 14(a)–14(c),
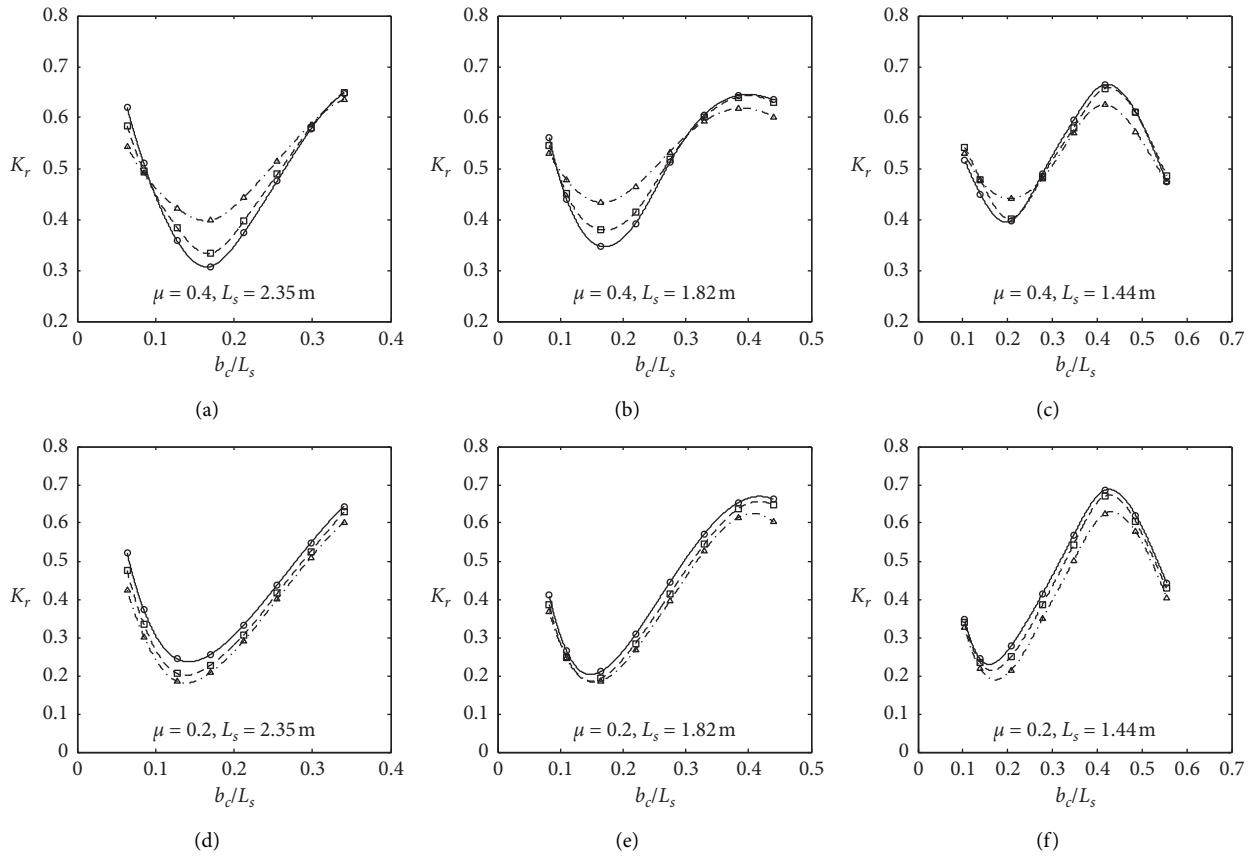
FIGURE 12: Reflection coefficients for irregular waves: ○, numerical results for $h_m = 0.10$ m; □, numerical results for $h_m = 0.15$ m; △, numerical results for $h_m = 0.20$ m.

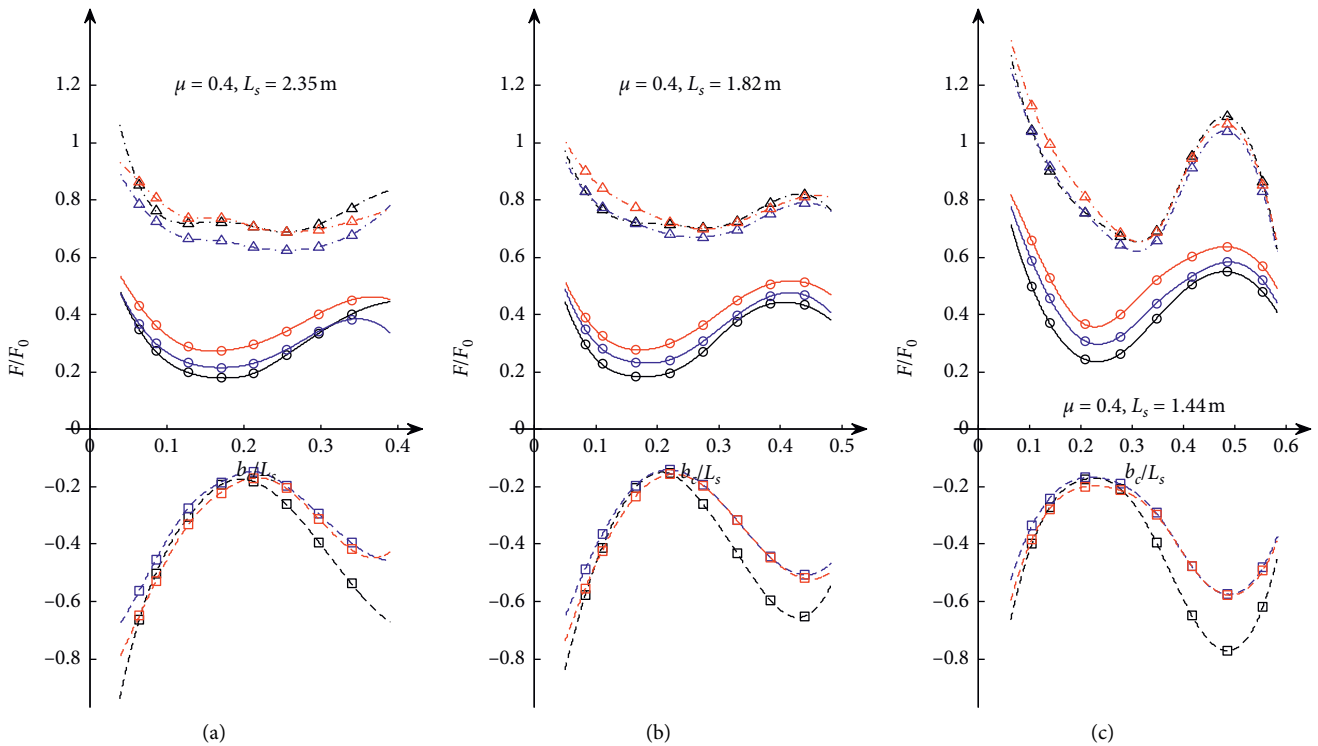FIGURE 13: Continued.

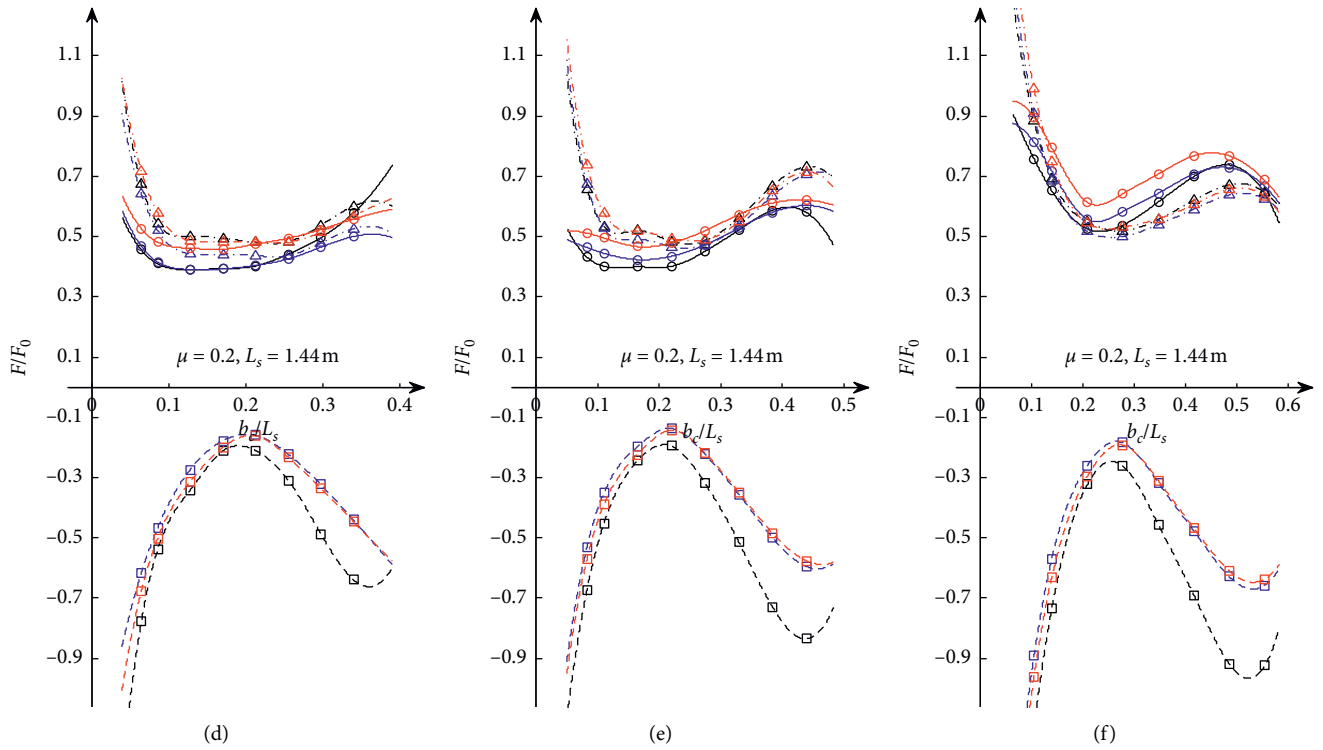(d)   (e)   (f)

Figure 13: Horizontal wave forces acting on each part of a perforated caisson for irregular waves: red ○, F_{h1}/F_{h0} for $h_m = 0.10$ m; blue ○, F_{h1}/F_{h0} for $h_m = 0.15$ m; black ○, F_{h1}/F_{h0} for $h_m = 0.20$ m; red □, F_{h2}/F_{h0} for $h_m = 0.10$ m; blue □, F_{h2}/F_{h0} for $h_m = 0.15$ m; black □, F_{h2}/F_{h0} for $h_m = 0.20$ m; red △, F_{h3}/F_{h0} for $h_m = 0.10$ m; blue △, F_{h3}/F_{h0} for $h_m = 0.15$ m; black △, F_{h3}/F_{h0} for $h_m = 0.20$ m.

(a)   (b)   (c)
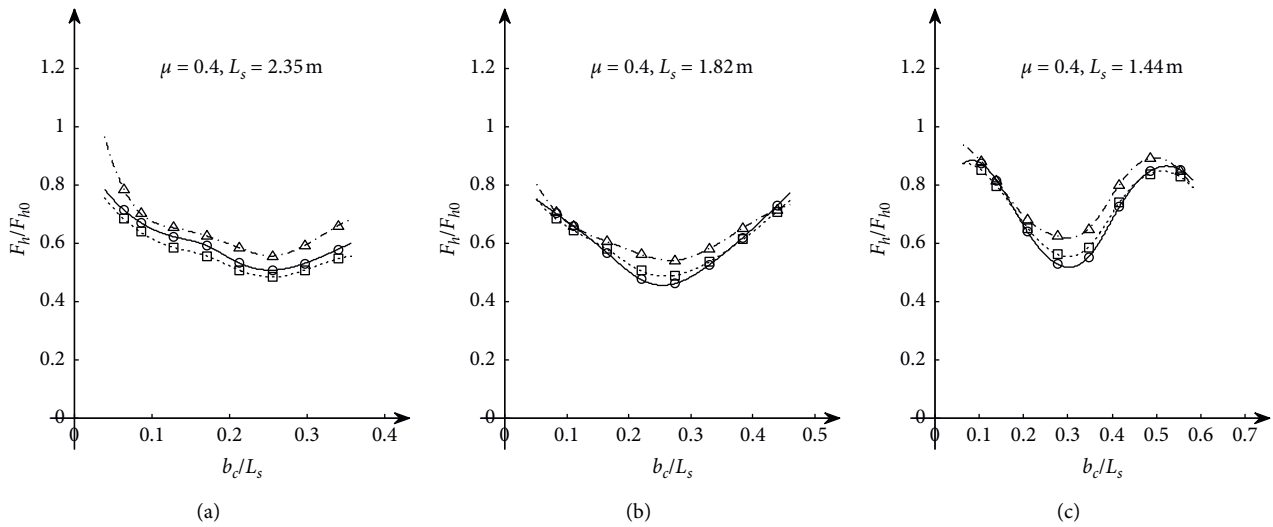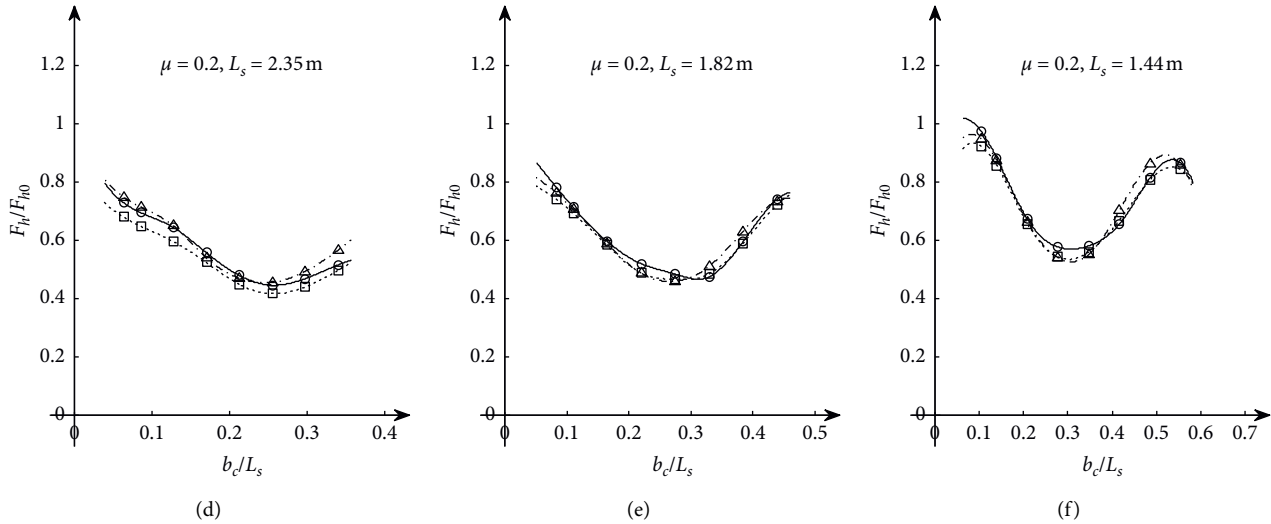
Figure 14: Continued.

FIGURE 14: Total horizontal wave force acting on the perforated caisson with irregular waves: black $\bigcirc$, F_h/F_{h0} for $h_m = 0.10$ m; black $\square$, F_h/F_{h0} for $h_m = 0.15$ m; black $\triangle$, F_h/F_{h0} for $h_m = 0.20$ m.

the perforation ratio was 0.4, and in Figures 14(d)–14(f), the perforation ratio was 0.2.

In Figure 14, as the wave-absorbing chamber width increased in a larger range, F_h/F_{h0} tended to oscillate in a decrease $\longrightarrow$ increase $\longrightarrow$ decrease manner, but the oscillation was weaker than for either F_{h1}/F_{h0} or F_{h2}/F_{h0}. The F_h/F_{h0} curve showed a certain amount of hysteresis compared with that of K_r. These were the common features regardless of the rubble-mound foundation height or the perforation ratio.

In addition, the variation of perforation ratio had almost no effect on the F_h/F_{h0} curve although the F_h/F_{h0} curve appeared to resemble the F_{h3}/F_{h0} curve more closely as the perforation ratio increased. This was mainly due to the greater force on the solid rear wall of the perforated caisson with greater perforation ratio.

Comparing the figures for different rubble-mound foundation heights, it could be found that the rubble-mound foundation height had limited influence on the total horizontal wave force. As in the figures for K_r, when the perforation ratio $\mu = 0.4$, the oscillation amplitudes became smaller with greater foundation heights, but this phenomenon was no longer evident when $\mu = 0.2$.

4. Conclusions

Model experiments were carried out to study the effects of a large range of the wave-absorbing chamber width on the wave attenuation performance of a perforated caisson sitting on a rubble-mound foundation. Meanwhile, a porosity-type numerical model based on VARANS equations was validated by comparing with the existing and present model experiments. The validated numerical model was then used for extended research. The conclusions are given as follows:

(i) The resistance-type porosity model used in the present research took into account the porosity of the rubble-mound foundation and the fluid viscosity. The numerical results were in good agreement with the existing and present model experiments. Therefore, the numerical model could be used to further study the wave interaction with a perforated caisson sitting on a rubble-mound foundation.

(ii) Resonant conditions occurred for various relative wave-absorbing chamber width introducing an oscillation in a decrease $\longrightarrow$ increase $\longrightarrow$ decrease manner of the reflection coefficients. This was a common feature regardless of the rubble-mound foundation height or the perforated ratio.

(iii) Resonant conditions occurred for various relative wave-absorbing chamber width introducing an oscillation in a decrease $\longrightarrow$ increase $\longrightarrow$ decrease manner of the horizontal wave forces acting on each part of the caisson. The horizontal wave force acting on the perforated front wall varied synchronously with the reflection coefficients, but the horizontal wave force acting on the solid rear back wall showed a certain amount of hysteresis.

(iv) Resonant conditions occurred for various relative wave-absorbing chamber width introducing an oscillation in a decrease $\longrightarrow$ increase $\longrightarrow$ decrease manner of the total horizontal wave force acting on the caisson. A certain amount of hysteresis was evident in the variation of the total horizontal wave force compared to that of the reflection coefficient.

(v) With the variation of the wave-absorbing chamber width, the reflection coefficient and horizontal wave force acting on a perforated caisson sitting on a rubble-mound foundation had minimum and maximum values. Considering the attenuation performance and wave force conditions, the wave-absorbing chamber should be neither too narrow nor too wide.

Data Availability

All the useful data including the experimental and numerical results used to support the findings of this study are included within the article. Other data are available upon request to Peihong Zhao (571509076@qq.com).

Conflicts of Interest

The authors declare that they have no conflicts of interest.

Acknowledgments

References

[1] G. E. Jarlan, "A perforated vertical wall breakwater," *The Dock and Harbour Authority*, vol. X11, no. 486, pp. 394–398, 1961.

[2] F. L. Terret, J. D. C. Osorio, and G. H. Lean, "Model studies of a perforated breakwater," in *Proceedings of the 11th Coastal Engineering Conference*, vol. 3, pp. 1104–1120, ASCE, London, UK, September 1968.

[3] M. Marks and G. E. Jarlan, "Experimental study on a fixed perforated breakwater," in *Proceedings of the 11th Coastal Engineering Conference*, vol. 3, pp. 1121–1140, ASCE, London, UK, September 1968.

[4] K. Tanimoto and L. Yoshimoto, "Theoretical and experimental study of reflection coefficient for wave dissipating caisson with a permeable front wall," *Report of the Port and Harbour Research Institute*, vol. 21, no. 3, pp. 44–77, 1982.

[5] R. Q. Li, "Hydraulic design method of wave dissipating structure with partially perforated," *Front wall China Ocean Engineering*, vol. 9, no. 1, pp. 73–82, 1995.

[6] X. F. Chen, Y. C. Li, D. P. Sun et al., "Experimental study of reflection coefficient and wave forces acting on perforated caisson," *Acta Oceanologica Sinica*, vol. 21, no. 3, pp. 451–460, 2002.

[7] X. F. Chen, Y. C. Li, Y. X. Wang et al., "Numerical simulation of wave interaction with perforated caisson breakwaters," *China Occan Engineering*, vol. 17, no. 1, pp. 33–43, 2003.

[8] X. Chen, Y. Li, and B. Teng, "Numerical and simplified methods for the calculation of the total horizontal wave force on a perforated caisson with a top cover," *Coastal Engineering*, vol. 54, no. 1, pp. 67–75, 2007.

[9] C. Stefania Ciocan, F. Taveira-Pinto, L. das Neves, and P. Rosa-Santos, "Experimental study of the hydraulic efficiency of a novel perforated-wall caisson concept, the LOWREB," *Coastal Engineering*, vol. 126, pp. 69–80, 2017.

[10] I. López, P. Rosa-Santos, C. Moreira, and F. Taveira-Pinto, "RANS-VOF modelling of the hydraulic performance of the LOWREB caisson," *Coastal Engineering*, vol. 140, pp. 161–174, 2018.

[11] X. F. Chen and R. Y. Chen, "An experimental study of wave acting on perforated caisson," *China Offshore Platform*, vol. 16, no. 5, pp. 1–6, 2001.

[12] B. Ma, *Wave Interaction with Perforated Caisson breakwater*, Dalian University of Technology, Dalian, China, 2004.

[13] J. Jiang, Y. Li, D. Sun et al., "Experimental study of the vertical wave forces acting on perforated caisson by irregular waves," *China Offshore Platform*, vol. 19, no. 5, pp. 7–14, 2004.

[14] J. Jiang, Y. Li, D. Sun et al., "Experimental study of calculating for wave forces acting on perforated caisson," *Port and Waterway Engineering*, vol. 30, no. 3, pp. 40–47, 2005.

[15] T. Xing, D. Sun, H. Wu et al., "Experimental investigation on reflection coefficient of perforated caisson with rubble foundation under action of irregular wave," *The Ocean Engineering*, vol. 34, no. 6, pp. 46–53, 2016.

[16] Y. Liu and Y. Li, "The reflection of regular and irregular waves by a partially perforated caisson breakwater on a step bed," *Acta Oceanologica Sinica*, vol. 28, no. 4, pp. 107–117, 2009.

[17] P. Zhao, D. Sun, and H. Wu, "Investigation on A Resistance-Type porosity model and the experimental coefficients," *China Ocean Engineering*, vol. 33, no. 4, pp. 468–476, 2019.

[18] A. Nakayama and F. Kuwahara, "A macroscopic turbulence model for flow in a porous medium," *Journal of Fluids Engineering*, vol. 121, no. 2, pp. 427–433, 1999.

[19] P. Frigaard and M. Christensen, "An absorbing wave-maker based on digital filters," *Coastal Engineering*, vol. 1995, pp. 168–180, 1994.

[20] P. Frigaard and M. Brorsen, "A time-domain method for separating incident and reflected irregular waves," *Coastal Engineering*, vol. 24, no. 3-4, pp. 205–215, 1995.

[21] W. Tang and D. Sun, "Numerical investigation of perforated caisson under the action of irregular wave," *The Ocean Engineering*, vol. 35, no. 4, 2017.

[22] Y. Goda, "A comparative review on the functional forms of directional wave spectrum," *Coastal Engineering Journal*, vol. 41, no. 1, pp. 1–23, 1999.

[23] Y. Goda and Y. Suzuki, "Estimation of incident and reflected waves in random wave experiments," in *Proceedings of the 15th Coastal Engineering Conference*, pp. 828–845, ASCE, Honolulu, HI, USA, July 1976.